RESEARCH ARTICLE

Ex uno plures: how to construct high-speed movies of collapsing cavitation bubbles from a single image

Armand Baptiste Sieber[1] · Davide Bernardo Preso[1] · Mohamed Farhat[1]

Abstract

The time-resolved visualization of the dynamics of a cavitation bubble usually requires the use of expensive high-speed cameras, which often provide a limited spatial resolution. In the present study, we propose an alternative to these high-speed imaging techniques. The method is based on the recently introduced virtual frame technique, which relates the motion of a monotonic propagating front to the resulting image blur captured on a long-exposure shadowgraph. We use a consumer-level camera to photograph the entire collapse phase of cavitation bubbles. We then demonstrate that both the dynamics of a spherically collapsing bubble and those of a bubble collapsing near a rigid boundary can be accurately reconstructed from this single photograph at a virtual frame rate of up to 2 Mfps on a 24.2 Mpx sensor.

1 Introduction

Cavitation bubbles are a topic of considerable interest because of the many processes in which they occur. While these bubbles are traditionally found in ship propellers and water turbines, where they cause noise, vibration and erosion (Arndt 2002; Amini et al. 2019), they are now also being progressively used in biomedical and cleaning applications, where their destructive properties are exploited (Stride and Coussios 2019; Yamashita and Ando 2019).

The study of the fundamental dynamics of these bubbles is often reduced to a simplified test case: the growth and collapse of a single bubble whose lifetime rarely exceeds a few milliseconds (Reuter and Mettin 2016; Supponen et al. 2019). This generally requires the use of high-speed cameras capable of capturing several hundred thousand frames per second or more. Commercially available high-speed cameras are not only financially restrictive, but also often have a limited spatial resolution and may only allow to record a limited number of frames. As an alternative, it has been shown that combining multiple images taken at different stages of the bubble lifetime allows reconstruction of the bubble behavior with a high spatial resolution (Vogel et al. 1996; Luo et al.

2020). This method however requires the generation of multiple cavitation bubbles and relies on the assumption that the successively observed bubbles exhibit a repeatable behavior. The need to create a multitude of bubbles to reconstruct their dynamics is alleviated if a multi-flash-per-camera-exposure imaging technique is used (Wilson et al. 2019; Sukovich et al. 2020; Agrež et al. 2020). With this technique, overlapping snapshots of the bubble profile are recorded on the imaging sensor, and an evaluation of the brightness level allows an unambiguous distinction of the bubble edge associated with each flash, provided that the bubble dynamics between flashes remains monotonic. On the other hand, optical methods employing laser deflection probes were also exploited to determine the radius evolution of spherical bubbles (Petkovšek and Gregorčič 2007) or of deformed bubbles near a rigid boundary (Gregorčič et al. 2008). Other methods used spatial transmission modulation techniques (Devia-Cruz et al. 2015) or interferometry (Wilson et al. 2021) to record the radial evolution of spherical cavitation bubbles. While these optical methods are less expensive than high-speed imaging and provide high temporal resolution, they do not allow a direct visual assessment of bubble shape.

In this work, we propose an alternative procedure to capture the collapse dynamics of a cavitation bubble. The method is based on the work of Dillavou et al. (2019), who described a novel imaging technique, termed the virtual frame technique (VFT), that exploits the bit-depth of any camera imaging sensor to relate the motion of a monotonically propagating front to the resulting blur captured on a

✉ Armand Baptiste Sieber
armand.sieber@epfl.ch

[1] Institute of Mechanical Engineering, École Polytechnique Fédérale de Lausanne, Avenue de Cour 33 Bis, 1007 Lausanne, Switzerland

shadowgraph. Taking advantage of the linear response of imaging sensors to incident light and setting thresholds for the brightness of the image pixels, the authors showed that the successive positions of a propagating front could be reconstructed within the camera's exposure time. In the following, we introduce a comprehensive procedure for employing the VFT with an off-the-shelf still camera and a specially designed single-pulse light source. With the help of a ray-tracing simulation, this procedure further demonstrates how to utilize the technique to capture the dynamics of laser-induced cavitation bubbles. Using this approach, we then successfully extract the bubble shape evolution for both spherical and non-spherical collapses with remarkable spatial and temporal resolutions. Finally, we evaluate the accuracy of the method by comparing the results to theoretical and numerical predictions as well as snapshots of similar bubbles taken at successive stages of their lifetime.

2 Materials and methods

2.1 Cavitation bubble generation

Single cavitation bubbles are generated by focusing a frequency-doubled Q-switched Nd:YAG pulsed laser in a $18 \times 18 \times 19$ cm transparent test chamber, filled with deionized water kept at room temperature. A schematic of the experimental setup is presented in Fig. 1a. The 8-ns and 532-nm laser pulse is first expanded to a diameter of 43 mm by a custom-made Galilean beam expander. It is then focused into water using an immersed aluminum off-axis parabolic mirror with a high convergence angle (45°) to generate a plasma from which the bubble emerges. The bubble lifetime is measured from the shock waves emitted upon bubble generation and collapses using a laser beam deflection probe. The system consists of a 15 mW, 532 nm continuous wave laser, whose beam is focused near the bubble generation site and whose intensity is monitored by a 1 ns rise time photodiode. Changes in the intensity of the laser beam not only allow the detection of shock waves, but also of a portion of the bubble growing and collapsing across the beam path. A characteristic signal recorded by the photodiode is shown in Fig. 1b.

Bubbles with a first oscillation period T of about 575 μs in an unbounded liquid are considered in this work. We demonstrated in a recent study (Sieber et al. 2022) that such bubbles exhibit a nearly symmetric growth and collapse phase and that their collapse dynamics can closely be approximated by the Rayleigh model (Rayleigh 1917). As such, the maximum radius of the bubble can be estimated from the duration of its first oscillation, which we consider to be twice the Rayleigh collapse time. It follows that $R_{\max} = T/1.83\sqrt{(p_0 - p_v)/\rho} \approx 3.1$ mm, where p_0 and p_v are the ambient pressure and vapor pressure, respectively, and ρ is the water density. Additionally, to characterize the proximity of the bubble to the solid boundary, we use the standoff parameter $\gamma = s/R_{\max}$, where s is the distance between the point of bubble generation and the boundary.
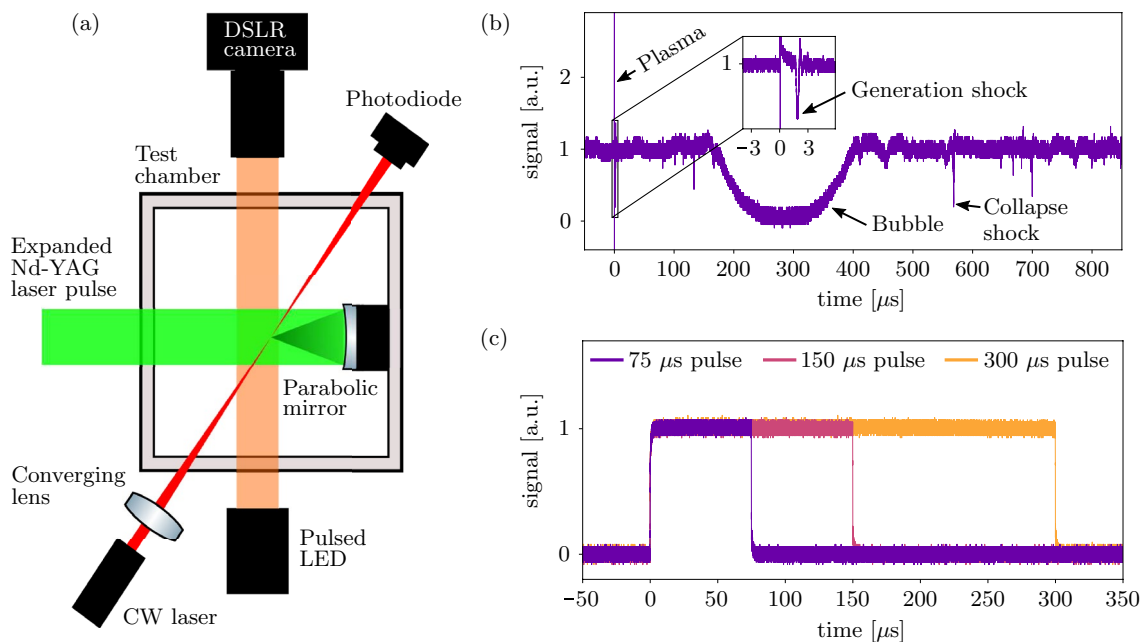

Fig. 1 **a** Schematic of the experimental setup. **b** Characteristic signal of the laser beam deflection probe and **c** signals of three LED light pulses of different lengths (75 μs, 150 μs and 300 μs), recorded with a fast rise time photodiode

In the case of the unbounded bubble, the nearest boundary is that of the parabolic mirror. Here, the standoff distance is $\gamma \approx 17.6$, which ensures a marginal influence of the mirror on the behavior of the bubble.

2.2 Imaging system

The dynamics of the bubble are captured on a single shadowgraph taken with a Nikon D5600 DSLR camera and backlit with the rectangular pulse of a collimated LED light source. These pulses are generated with a custom-made system. It consists of a single LED with a dominant wavelength of 617 nm (OSRAM OSCONIQ P 3030). The LED has a nominal forward voltage of 2.2V and forward current of 350mA. It is however powered by a 12V power supply capable of providing up to 2A of current. By supplying power beyond its rated operating conditions, the LED can emit significantly more light for brief pulses without being damaged (Willert et al. 2012). The LED is connected to an IRF520 MOSFET driver module. The MOSFET is a field-effect transistor that we use as a switch to turn the LED on and off with an external 5V signal provided by a delay generator, allowing a precise modulation of the signal length and delay with respect to the bubble generation. Photodiode signals of a 75 μs, 150 μs, and 300 μs light pulses are presented in Fig. 1b. The constant light intensity is not affected by the duration of the pulse and has extremely short rise times ($\sim$750 ns) and fall times ($\sim$500 ns).

The DSLR camera has a 24.2 million pixels CMOS sensor (6016×4016 pixels). It is equipped with a 105 mm lens and a 2× teleconverter to achieve a spatial resolution of 2 μm/pixel. The experiment is conducted in a darkened room, and the shutter of the camera is opened before the bubble is created and left open for the entire measurement sequence. This however leaves the camera's sensor exposed to the bright glow of the laser plasma. To block out this light and avoid saturation, we use a 570 nm long-pass filter and a 2.0 neutral density filter on the camera lens. We illustrate in Fig. 2 the ability of the different filters to block out the plasma light. In Fig. 2a, no filter is used and the green glow of the generation plasma significantly affects the overall image. Using only the long-pass filter (Fig. 2b), most of the green laser light is removed, but a substantial portion of the plasma is still visible. With the additional neutral density filter, the image appears completely dark (Fig. 2c). Figure 2d shows the red channel pixel intensity of the RGB images along the line indicated by the arrow. While both the image without the filter and the image with the long-pass filter are saturated around the plasma point, the addition of the neutral density filter effectively reduces the impact of the laser plasma. Indeed, only a small part of the camera sensor is affected by a slight increase in pixel intensity at the plasma point, while the signal merges with the background noise
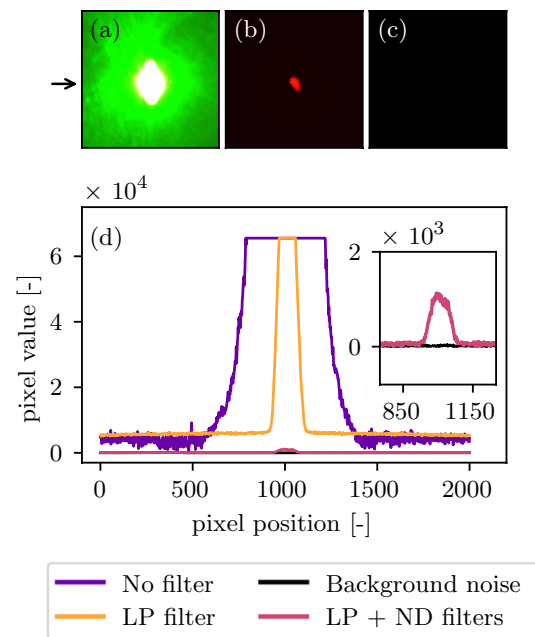

Fig. 2 RGB photographs of the laser plasma glow taken **a** without protection filter, **b** with a 570 nm long-pass filter (LP) and **c** with a 570 nm long-pass filter and a 2.0 neutral density filters (ND). **d** Red channel pixel intensities along the position marked by the arrow. These values are compared to the background noise of the imaging sensor, measured in a similar environment in the absence of plasma generation

everywhere else. As a result, the exposure of the camera sensor to light is solely determined by the LED pulse.

Furthermore, given the cut-on wavelength of the long-pass filter and the peak wavelength of the illumination source, only the red channel of the photographed RGB images can be considered for processing and analysis. Also, unless otherwise specified, all images are taken at an ISO 100 setting (light sensitivity of the camera sensor) and saved as RAW files to avoid in-camera processing such as white balance or hue adjustment. The RAW images are then converted in Python to linear 16-bit images in Tag Image File Format (TIFF) using the Rawpy wrapper for the LibRaw library (Riechert 2014).

We finally assess the pixels response to light by gradually increasing the duration of the LED pulses and retrieving the red channel value of each pixel. For this process, we only consider central area of the imaging sensor (4000×4000 pixels), where the bubble is imaged. Figure 3 shows the intensity response of the pixel with the steepest response, the pixel with the flattest response and a pixel with the mean response. The different slopes are due to the spatial variation of the LED illumination profile, with the steepest slope relating to a central pixel of the camera sensor where the intensity of the light pulse is brightest. Overall, all pixels responses are very well approximated by linear regressions
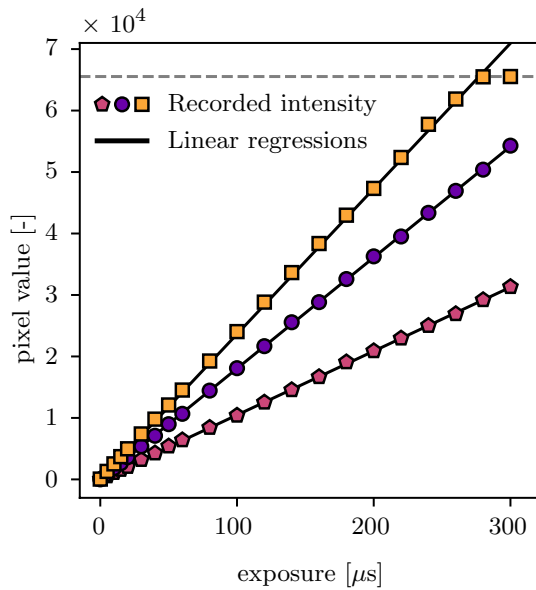
Fig. 3 Intensity response of the red channel pixel values as a function of the LED pulses duration. The different curves refer to three different pixels of the imaging sensor: pixel with the steepest response (square markers), the pixel with the flattest response (pentagon markers) and a pixel with the mean response (circular markers). The linear regressions highlight the linear behavior of the imaging sensor and the dashed gray line shows the saturation value of the 16-bit images

with an average coefficient of determination of $R^2 = 0.99998$ and a minimum value of $R^2 = 0.99865$.

2.3 Bubble dynamics reconstruction

The duration of the light pulse, τ, is chosen to cover most of the cavitation bubble's collapse phase. Consequently, the fast-moving front of the bubble leads to a blurred image, characterized by a gradient of the pixels intensity. To translate this blur into temporal information, we use the virtual frame technique (VFT) (Dillavou et al. 2019). The VFT is based on the premise that the instantaneous light intensity reaching each pixel is binary, i.e., a pixel is either illuminate by the light source or obscured by the shadow of the collapsing bubble. Furthermore, the collapse of the photographed bubble is monotonic. This implies that any pixel obscured by the bubble shadow at the beginning of the exposure can only transition once to illuminated. The time of this transition is noted $t_{m,n} \in [0, \tau]$, where m refers the mth row and n to the nth column of the imaging sensor pixel array. Since the camera sensors' response to incident light is linear, the intensity of each pixel is consequently determined by the following equation:

$$I_{m,n} = a_{m,n}(\tau - t_{m,n}) + b_{m,n}t_{m,n} + I_{\text{noise},m,n} \quad (1)$$
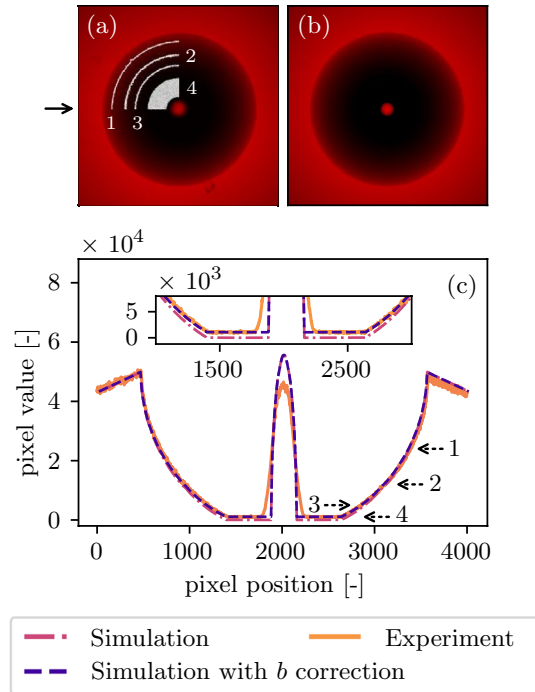

Fig. 4 **a** Long-exposure shadowgraph of a cavitation bubble collapsing in an unbounded medium with selected contour lines of the pixel intensities (1-4) and **b** synthetic shadowgraph of the same bubble constructed from the ray-tracing simulation. **c** Pixel intensity along the line indicated by the solid arrow for the shadowgraph, the numerical simulation and the simulation corrected with response curve b for the obscured pixels. The various dashed arrows indicate the position of the contour lines (1-4) displayed on subfigure (**a**)

where a and b are the intensity response of pixels when illuminated by the LED pulse and when obscured by the bubble shadow, respectively, and I_{noise} is an offset that accounts for the background noise on the camera sensor in the absence of light pulse. Both a and I_{noise} are derived from the linear regressions performed on each pixel, as shown in Fig. 3. We determine the value of b by measuring the intensity of the pixels obscured by the bubble's shadow. Equation 1 can then be rewritten to map the transition time of each pixel from dark to illuminated,

$$t_{m,n} = \frac{I_{m,n} - a_{m,n}\tau - I_{\text{noise},m,n}}{b_{m,n} - a_{m,n}} \quad (2)$$

By setting thresholds on the transition time, the shape of the bubble can be reconstructed at any stage of its collapse. It is worth noting here that, in the case where the illumination source is perfectly uniform, the indices may be omitted as the intensity response would be identical for all pixels.

We use Fig. 4 to detail the procedure for estimating the value of b. Figure 4a shows a long-exposure shadowgraph of a bubble with a collapse time of 294 μs and backlit with a 270 μs LED pulse, triggered so that the illumination ends 17

μs before the bubble collapses. Four contour lines of equal pixel intensity are additionally displayed on one quarter of the bubble. Contours 1, 2 and 3 indicate the position of the bubble wall at various stages of its collapse, while the thicker fourth contour maps the pixels that were obscured from light throughout the exposure, indicating the position and shape of the bubble at this final stage. This last contour is cut off by a bright spot in the center of the bubble. It is the result of a portion of the light beam which crosses the bubble without significant reflection or refraction before reaching the imaging sensor. Given the symmetry of the bubble dynamics, the presence of this bright spot does not affect the output of the VFT, provided that the bubble remains larger than the spot size throughout the exposure. For visual purposes, the shadowgraph may therefore even be retouched and the bright spot removed without compromising the temporal information it contains. The fourth contour has a fairly homogeneous minimum intensity level $\min(I_{m,n}) \approx 1050$. This intensity is almost two orders of magnitude greater than I_{noise}, indicating that light is reaching the pixels obscured by the bubble's shadow. This light emission may either be attributed to a scattering of the LED pulse by the bubble or by elements in its vicinity. To determine its origin, we use a ray-tracing simulation to reproduce the shadowgraph shown in Fig. 4a. The simulation procedure is inspired by the work of Senegačnik et al. (2021) and is implemented as follows. The bubble is regarded as a two-dimensional cavity filled with air. It is immersed in a water tank with similar dimensions as in the experiment and illuminated with an ideally collimated, planar light beam whose intensity profile corresponds to that of the LED. The refractions and reflections of light at the interfaces of the bubble and at the walls of the water tank are determined by Snell's law. After their initial refraction at the liquid-air interface of the bubble, the incident light rays are successively split into a refracted and a reflected component. We limit this process to five consecutive splittings so that most of the light scattered by the bubble is resolved. The initial refraction of an incident light ray at the bubble interface and the first three splittings are illustrated in Fig. 5. The intensity evolution of the two resulting ray components is determined by Fresnel's equations for unpolarized light. In turn, a portion of the rays that exit the bubble and the water tank reach the camera lens. The latter is modeled as a thin lens whose focal length is identical to that of the actual lens and whose size is determined by the aperture used in the experiment. Finally, these rays form an image on a synthetic sensor, which is taken as a line of pixels that have a size and spacing derived from the DSLR camera's sensor. The distance between the lens and the sensor is determined using the thin lens equation and the distance between the lens and the bubble is chosen so that the magnification ratio obtained with the synthetic camera corresponds to that of the experiment. We consider several
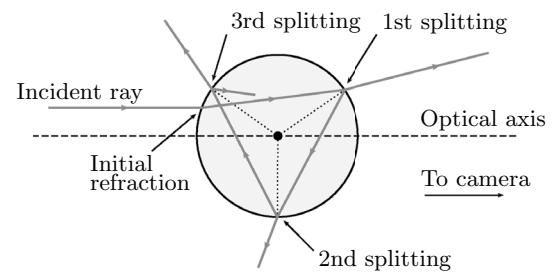

Fig. 5 Reflection and refraction of an incident light ray at an air-filled spherical cavity immersed in water. After the initial refraction, the ray is split five times in succession into a refracted and a reflected component. For clarity, only the first three splittings are sketched in the figure. The initial reflection is also omitted from the sketch

successive instants of the bubble collapse phase, whose radius is dictated by Rayleigh's model, and run as many ray-tracing simulations to create the final synthetic long-exposure shadowgraph. The resulting image, reconstructed from the pixel line taking into account the spherical symmetry, is shown in Fig. 4b. In Fig. 4c, we show the pixel intensity along the line indicated by the solid arrow. Both curves feature a central peak in pixel intensity that corresponds to the bright spot visible in the shadowgraphs. Additionally, the fourth contour, characterized by $\min(I_{m,n}) \approx 1050$, is clearly visible on the experimental intensity curve. The simulation also predicts such a plateau, but with an intensity value close to 0. This suggests that the scattering of the light pulse by the bubble alone cannot explain why light reaches the obscured pixels in the experiment. Other factors must therefore be considered, including unwanted reflections of the LED pulse from surfaces near the bubble or scattering of the light by the filters in front of the camera lens and in the lens system of the camera itself. The latter is referred as *veiling glare* and can cause a global illumination effect on the image plane, thus reducing contrast (Matsuda and Nitoh 1972; Talvala et al. 2007). To include this effect in the simulation, we assume that it affects all pixels equally and model it by assigning a nonzero intensity response curve to all pixels that are obscured by the bubble shadow. The value of this response curve is derived from Eq. 1 for the fourth intensity contour and is given by the following average value $b_{\text{min, avg}} = (\min(I_{m,n}) - I_{\text{noise,avg}})/\tau$. When illuminated by the light pulse, the pixels do not need this correction, as any light scattering in the absence of the bubble would have already been accounted for in the pixels response curves given by a. The resulting intensity profile is also included in Fig. 4c, which shows a remarkable agreement with the experiment. This suggests that an effect similar to the *veiling glare* is likely to explain why the pixels obscured by the bubble shadow are not completely dark. This also provides a solid basis for assuming that b can be taken as constant for all pixels during bubble collapse and that its value can be

derived from the minimum measured intensity contour, as it was done in the simulation. Therefore, $b_{\mathrm{min, avg}}$ will be used instead of $b_{m,n}$ in Eq. 2.

3 Results and discussion

We apply the imaging procedure described above to two test cases: the spherical collapse of a bubble in an unbounded medium and the collapse of a bubble near a rigid boundary. We then compare the reconstructed bubble dynamics with short-exposure shadowgraphs of similar bubbles captured on the same DSLR camera and backlit with very short LED pulses (FWHM ~350 ns). These bubbles have a lifetime that differs by less than 0.4% from the lifetime of the bubble captured in the long-exposure photos, resulting in a similar deviation for the maximum bubble radius measured in our experiment. We therefore consider that a direct comparison of the dimensionless evolution of the radii of the different bubbles is possible and allows an evaluation of the accuracy of the visualization technique.

3.1 Spherical bubble collapse

In Fig. 6, we present the dynamics of a spherically collapsing cavitation bubble. Figure 6a shows the original long-exposure shadowgraph next to a retouched image where the central bright spot has been removed for visual purposes. The photographed bubble has a total lifetime of 574.4 μs and is illuminated with a light pulse of 270 μs triggered 300 μs after the bubble generation. Five images reconstructed from long-exposure shadowgraph using Eq. 2 show different instants of the bubble collapse in Fig. 6b. In Fig. 6c, we systematically compare these reconstructions with short-exposure snapshots of similar bubbles taken at the same dimensionless times, $t^* = t/T_{1/2}$, where the quantity $T_{1/2}$ represents the half-life of the bubble. It should be noted that the short-exposure photographs were taken at an ISO setting of 8000 (as opposed to the ISO setting of 100 for the long-exposure shadowgraphs), which explains why the generation plasma is visible at the center of the bubble. A comparison between the two sets of images highlights a close qualitative resemblance. Figure 6d shows the dimensionless time

Fig. 6 **a** Long-exposure shadowgraph of a cavitation bubble collapsing in an unbounded medium: original and retouched images. **b** Selected instants of the bubble collapse reconstructed from the long-exposure shadowgraphs and **c** short-exposure baseline snapshots of the bubble taken at same dimensionless time: (1) $t^* \approx 1.05$, (2) $t^* \approx 1.26$, (3) $t^* \approx 1.51$, (4) $t^* \approx 1.73$ and (5) $t^* \approx 1.96$. **d** Normalized temporal evolution of the bubble radius
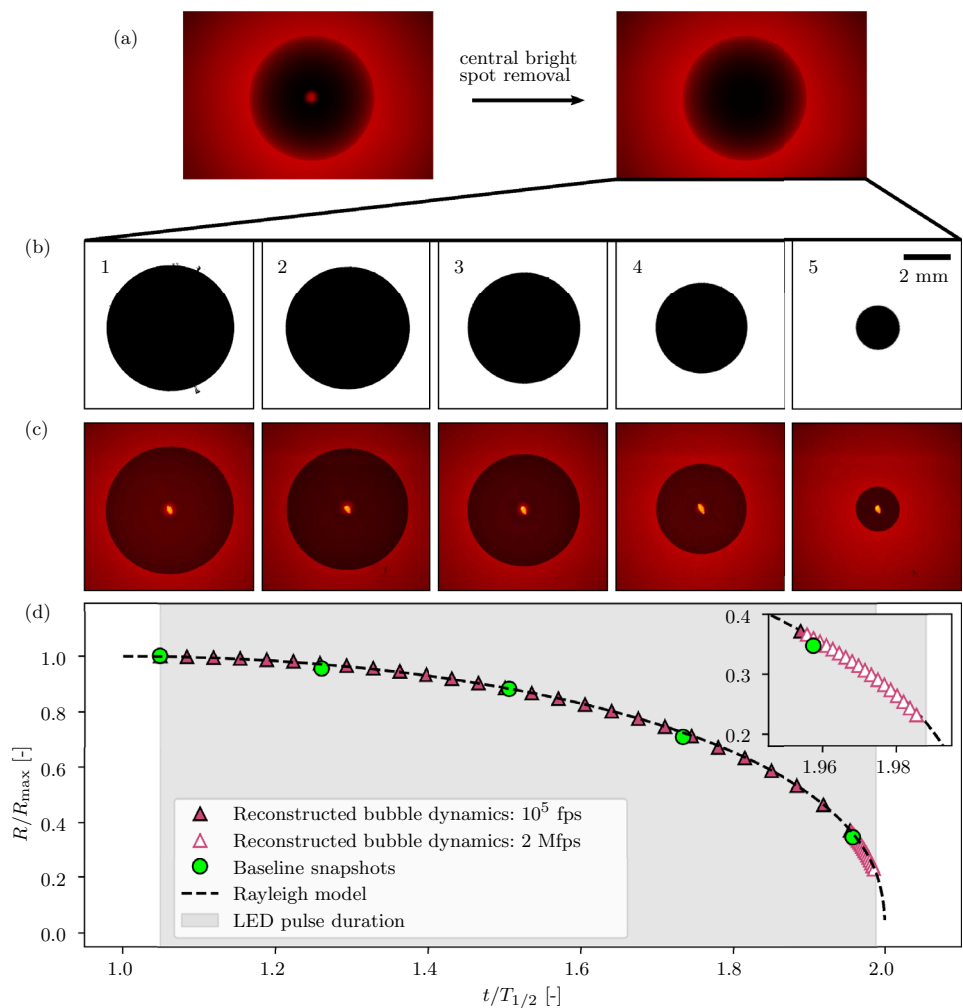
evolution of the bubble radius, normalized by the bubble maximum radius R_{max}. Both the radii from the long-exposure shadowgraph and the baseline snapshots are shown alongside the theoretical prediction of the Rayleigh model, where the collapse of a spherical cavity filled with liquid vapor of constant pressure $p_v = 2300$ Pa is considered in an inviscid and incompressible liquid at rest. Filled triangular markers represent the bubble radii extracted from a reconstructed virtual frame rate of 10^5 frames per second, while the hollow markers are taken from a $2 \cdot 10^6$ frames per second reconstruction. The reconstructed bubble radius evolution agrees well with that of the baseline snapshots and with the theoretical prediction of the Rayleigh model. We note that the relative difference between the radii calculated from the reconstructed images and the baseline snapshots is no more than 2%. Furthermore, this imaging technique enables the reconstruction of the bubble dynamics over ~ 99.6% of the exposure time, i.e., ~269 μs, as highlighted in the zoomed region of Fig. 6d. A reconstruction over the entire 270 μs is hindered because no clear distinction of the bubble boundary is possible in the last instants of the

exposure time. We believe this is due to a combination of factors, including the nonzero rise and fall times of the light pulse and noise in the light beam and on the camera sensor.

3.2 Aspherical bubble collapse

In Fig. 7, we present the collapse dynamics of a bubble near a rigid boundary. The bubble under investigation is generated at a standoff distance $\gamma \approx 1.25$ from the boundary and has a total lifetime of 643.6 μs. We illuminate it with a light pulse of 270 μs triggered 360 μs after the bubble generation. These values are chosen to ensure that only the collapse phase is captured and that the microjet, which forms when a bubble collapses near a rigid boundary, does not pierce the bubble's lower hemisphere before the end of the light pulse. Thus, we are only photographing a monotonic process. In Fig. 7a, we show the long-exposure shadowgraph and the retouched equivalent image without the central bright spot. The rigid boundary casts a diffuse shadow on the image. At $\gamma \approx 1.25$, this has no impact on the intensity responses $a_{m,n}$ of the pixels covering the dynamics of the bubble. However,

Fig. 7 **a** Long-exposure shadowgraph of a cavitation bubble collapsing near a solid boundary at $\gamma \approx 1.25$: original and retouched images. **b** Selected instants of the bubble collapse reconstructed from the long-exposure shadowgraphs and **c** short-exposure baseline snapshots of the bubble taken at same dimensionless time: (1) $t^* \approx 1.12$, (2) $t^* \approx 1.33$, (3) $t^* \approx 1.53$, (4) $t^* \approx 1.73$ and (5) $t^* \approx 1.93$. **d** Normalized temporal evolution of the bubble equivalent radius
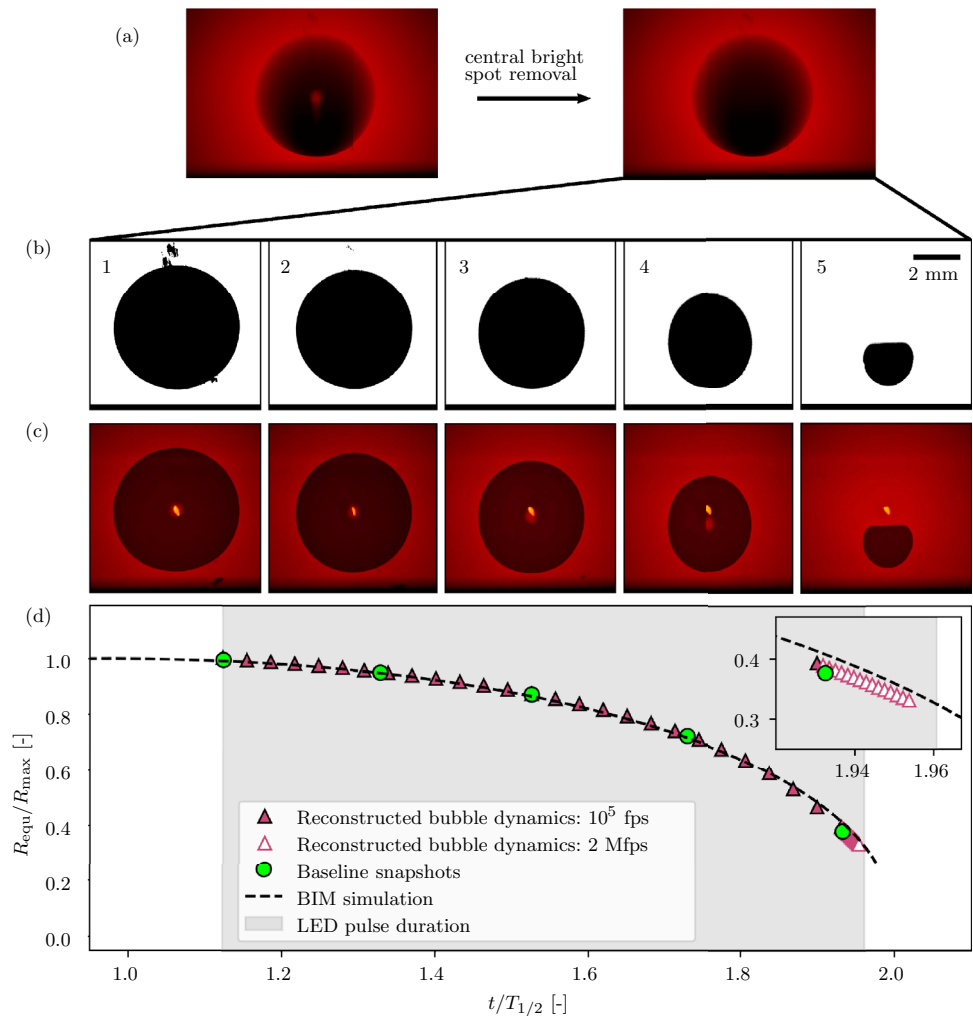
should the bubble be generated closer to the boundary, new intensity responses would have to be measured to account for this effect. Figure 7b shows five reconstructed images illustrating different moments of the bubble collapse. These images are juxtaposed with the short-exposure snapshots, taken at the same dimensionless time t^*, in Fig. 7c. A comparison between the two visualization techniques shows a remarkable qualitative correspondence and highlights the significant difference between the collapse dynamics of a bubble in an unbounded medium and that of a bubble developing near a rigid boundary. In addition, we present in Fig. 7d the temporal evolution of the bubble equivalent radii R_{equ}, computed from the projected area A_p as $R_{equ} = \sqrt{A_p/\pi}$. For the sake of completeness, this figure also shows the numerical solution of the boundary integral method (BIM) for a bubble collapsing near a rigid boundary at $\gamma = 1.25$. Details of this potential flow solver can be found in references (Sieber et al. 2022, 2023). The reconstructed bubble dynamics, indicated by hollow and filled triangular markers, agree very well with the baseline snapshots, indicated by circular markers, as well as with the predictions of the numerical model. The relative difference in estimated radius between the reconstructed frames and the baseline snapshots is less than 2%. In addition, we manage to reconstruct the bubble dynamics over ~99.1% of the exposure time, i.e., ~267.5 μs). As with the spherically collapsing bubble, a clear determination of the bubble boundary beyond this point prevents the reconstruction of its dynamics.

Another key feature of the bubble dynamics near rigid boundaries is the displacement of its centroid. We therefore present in Fig. 8 the normalized displacement of the bubble center of mass, $z^* = z/R_{max}$, where z represents the distance between the bubble centroid and the rigid boundary. A normalized displacement of $z^* = \gamma$ would thus mean that the center of gravity of the bubble has not moved, while a displacement of $z^* = 0$ would imply that the bubble's centroid has migrated to the very surface of the rigid boundary. To measure this displacement, we consider two different reconstructed virtual frame rates: 10^5 frames per second to cover the overall behavior of the bubble collapse and $2 \cdot 10^6$ frames per second to capture the final phase of this collapse. In addition, we include in Fig. 8 the displacements measured from the short-exposure snapshots and computed in the numerical simulation. As for the temporal evolution of the bubble radius, we observe a strong agreement between the two sets of measurements, where the maximum relative difference is barely more than 2.1%.

3.3 Advantages and limitations

The remarkable agreement between the reconstructed dynamics and the baseline snapshots demonstrates the
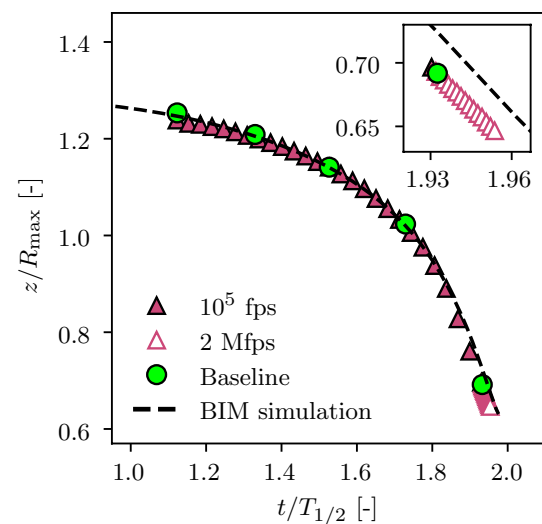

Fig. 8 Normalized displacement of the bubble center of mass

applicability and quality of the imaging procedure presented in this work.

Nevertheless, we would like to point out that the method suffers from two major limitations. First, only monotonic processes can be reconstructed, which means that only purely growing or collapsing phases of the bubble can be photographed. However, with a basic knowledge of the bubble behavior in combination with the information provided by the laser beam deflection probe, this drawback can be managed and the desired instants of the bubble lifetime can be photographed exactly. Secondly, the presence of a bright light spot in the center of the bubble limits the minimum resolvable bubble radius. In the case of the spherically collapsing bubble studied in this work, this radius would be about 0.5 mm, which corresponds to a ratio $R/R_{max} \approx 0.16$. According to Rayleigh model, the bubble reaches this radius at $t^* = t/T_{1/2} \approx 1.9945$. In dimensional term, where $T_{1/2} = 287.2$ μs for the bubble considered in Sect. 3.1, this means that roughly 1.6 μs would elapse between the minimum resolvable radius and the collapse of the bubble. To put this limitation into perspective, one should consider that a time-resolved visualization of the events in between would require a high-speed camera capable of capturing at least 625,000 frames per second.

The method also offers valuable advantages over conventional imaging techniques. First, the high spatial resolution of the DSLR camera allows a detailed visualization of the bubble behavior. At its maximum expansion, the radius of the bubble shown in Sect. 3.1 is resolved by ~1500 pixels, while at its minimum size, the radius is resolved by ~350 pixels. Second, the method provides a fine time-resolved reconstruction of the bubble behavior. The minimum time step that can be reconstructed depends on the smallest resolvable step in pixel intensity, $\Delta t_{min} = \Delta I_{min}/(b-a)$,

where the subscripts have been omitted for clarity (c.f. Eq. 2). In the case of the bubbles studied in this work, a virtual frame rate as high as 2 million frames per second may be reached to follow the bubble motion without being significantly affected by noise. With such impressive performance, the VFT technique may replace or complement conventional high-speed cameras to visualize the rapid motion of cavitation bubbles. For example, the imaging procedure presented here could be used to observe the final moments of a bubble's collapse, enhancing our ability to measure the bubble's fast dynamics that take place within these final instants.

4 Conclusion

In this work, we have presented a detailed imaging procedure to track the rapid motion of a laser-induced cavitation bubble using only a consumer-level camera and a custom-built rectangular light pulse generator. The results show that the dynamics of a spherically collapsing bubble and those of a bubble collapsing near a rigid boundary can be accurately recovered with a very high temporal resolution of 2 million virtual frames per second on a 24.2 Mpx imaging sensor. These promising results will hopefully pave the way for this imaging technique to be used as an alternative or complement to conventional high-speed cameras in the study of cavitation bubbles.

Author contributions ABS and MF developed the original idea. MF acquired the funding and supervised the project. ABS and DBP conducted the experiments. ABS analyzed the data and wrote the ray-tracing solver with inputs of MF and DBP. The manuscript was written by ABS with the help of MF and DBP. All authors reviewed the manuscript.

Data availability The data that support the findings of this study are available from the corresponding author upon reasonable request.

Declarations

Conflict of interest The authors report no conflict of interest.

Ethical approval Not applicable.

References

Agrež V, Požar T, Petkovšek R (2020) High-speed photography of shock waves with an adaptive illumination. Opt Lett 45(6):1547–1550. https://doi.org/10.1364/OL.388444

Amini A, Reclari M, Sano T, Iino M, Farhat M (2019) Suppressing tip vortex cavitation by winglets. Exp Fluids 60:1–15. https://doi.org/10.1007/s00348-019-2809-z

Arndt RE (2002) Cavitation in vortical flows. Annu Rev Fluid Mech 34(1):143–175. https://doi.org/10.1146/annurev.fluid.34.082301.114957

Devia-Cruz LF, Camacho-López S, Cortés VR, Ramos-Muñiz V, Pérez-Gutiérrez FG, Aguilar G (2015) Reconstruction of laser-induced cavitation bubble dynamics based on a Fresnel propagation approach. Appl opt 54(35):10432–10437. https://doi.org/10.1364/AO.54.010432

Dillavou S, Rubinstein SM, Kolinski JM (2019) The virtual frame technique: ultrafast imaging with any camera. Opt Express 27(6):8112–8120. https://doi.org/10.1364/OE.27.008112

Gregorčič P, Petkovšek R, Možina J, Močnik G (2008) Measurements of cavitation bubble dynamics based on a beam-deflection probe. Appl Phys A 93(4):901–905. https://doi.org/10.1007/s00339-008-4751-4

Luo JC, Ching H, Wilson BG, Mohraz A, Botvinick EL, Venugopalan V (2020) Laser cavitation rheology for measurement of elastic moduli and failure strain within hydrogels. Sci Rep 10(1):1–13. https://doi.org/10.1038/s41598-020-68621-y

Matsuda S, Nitoh T (1972) Flare as applied to photographic lenses. Appl Opt 11(8):1850–1856. https://doi.org/10.1364/AO.11.001850

Petkovšek R, Gregorčič P (2007) A laser probe measurement of cavitation bubble dynamics improved by shock wave detection and compared to shadow photography. J Appl Phys 102(4):044909. https://doi.org/10.1063/1.2774000

Rayleigh L (1917) On the pressure developed in a liquid during the collapse of a spherical cavity. London Edinburgh Dublin Philos Mag J Sci 34(200):94–98. https://doi.org/10.1080/14786440808635681

Reuter F, Mettin R (2016) Mechanisms of single bubble cleaning. Ultrason Sonochem 29:550–562. https://doi.org/10.1016/j.ultsonch.2015.06.017

Riechert M (2014) Raw image processing for python, a wrapper for libraw. (Date accessed: 01/12/2022) https://github.com/letmaik/rawpy

Senegačnik M, Kunimoto K, Yamaguchi S, Kimura K, Sakka T, Gregorčič P (2021) Dynamics of laser-induced cavitation bubble during expansion over sharp-edge geometry submerged in liquid-an inside view by diffuse illumination. Ultrason Sonochem 73(105):460. https://doi.org/10.1016/j.ultsonch.2021.105460

Sieber AB, Preso DB, Farhat M (2022) Dynamics of cavitation bubbles near granular boundaries. J Fluid Mech 947:A39. https://doi.org/10.1017/jfm.2022.698

Sieber AB, Preso D, Farhat M (2023) Cavitation bubble dynamics and microjet atomization near tissue-mimicking materials. Phys Fluids 35(2):027101. https://doi.org/10.1063/5.0136577

Stride E, Coussios C (2019) Nucleation, mapping and control of cavitation for drug delivery. Nat Rev Phys 1(8):495–509. https://doi.org/10.1038/s42254-019-0074-y

Sukovich JR, Haskell SC, Xu Z, Hall TL (2020) A cost-effective, multi-flash, ghost imaging technique for high temporal and spatial resolution imaging of cavitation using still-frame cameras. J Acoustic Soc Am 147(3):1339–1343. https://doi.org/10.1121/10.0000802

Supponen O, Obreschkow D, Kobel P, Dorsaz N, Farhat M (2019) Detailed experiments on weakly deformed cavitation bubbles. Exp Fluids 60:1–13. https://doi.org/10.1007/s00348-019-2679-4

Talvala EV, Adams A, Horowitz M, Levoy M (2007) Veiling glare in high dynamic range imaging. ACM Trans Graph (TOG) 26(3):37. https://doi.org/10.1145/1276377.1276424

Vogel A, Busch S, Parlitz U (1996) Shock wave emission and cavitation bubble generation by picosecond and nanosecond optical breakdown in water. J Acoustic Soc Am 100(1):148–165. https://doi.org/10.1121/1.415878

Willert CE, Mitchell DM, Soria J (2012) An assessment of high-power light-emitting diodes for high frame rate schlieren imaging. Exp Fluids 53(2):413–421. https://doi.org/10.1007/s00348-012-1297-1

Wilson BG, Fan Z, Sreedasyam R, Botvinick EL, Venugopalan V (2021) Single-shot interferometric measurement of cavitation bubble dynamics. Opt Lett 46(6):1409–1412. https://doi.org/10.1364/OL.416923

Wilson CT, Hall TL, Johnsen E, Mancia L, Rodriguez M, Lundt JE, Colonius T, Henann DL, Franck C, Xu Z et al (2019) Comparative study of the dynamics of laser and acoustically generated bubbles in viscoelastic media. Phys Rev E 99(4):043103. https://doi.org/10.1103/PhysRevE.99.043103

Yamashita T, Ando K (2019) Low-intensity ultrasound induced cavitation and streaming in oxygen-supersaturated water: role of cavitation bubbles as physical cleaning agents. Ultrason Sonochem 52:268–279. https://doi.org/10.1016/j.ultsonch.2018.11.025